crystals

MDPI

Article

Luminescence Efficiency of Cerium Bromide Single Crystal under X-ray Radiation

Dionysios Linardatos [1,*], Christos Michail [1], Nektarios Kalyvas [1], Konstantinos Ninos [2], Athanasios Bakas [2], Ioannis Valais [1], George Fountos [1] and Ioannis Kandarakis [1]

[1] Radiation Physics, Materials Technology and Biomedical Imaging Laboratory, Department of Biomedical Engineering, University of West Attica, Ag. Spyridonos, 12210 Athens, Greece; cmichail@uniwa.gr (C.M.); nkalyvas@uniwa.gr (N.K.); valais@uniwa.gr (I.V.); gfoun@uniwa.gr (G.F.); kandarakis@uniwa.gr (I.K.)
[2] Department of Biomedical Sciences, University of West Attica, Ag. Spyridonos, 12210 Athens, Greece; kninos@uniwa.gr (K.N.); abakas@uniwa.gr (A.B.)
* Correspondence: dlinardatos@uniwa.gr

Abstract: A rare-earth trihalide scintillator, $CeBr_3$, in 1 cm edge cubic monocrystal form, is examined with regard to its principal luminescence and scintillation properties, as a candidate for radiation imaging applications. This relatively new material exhibits attractive properties, including short decay time, negligible afterglow, high stopping power and emission spectrum compatible with several commercial optical sensors. In a setting typical for X-ray radiology (medical X-ray tube, spectra in the range 50–140 kVp, human chest equivalent filtering), the crystal's light energy flux, absolute efficiency (AE) and X-ray luminescence efficiency (XLE) were determined. Light energy flux results are superior in comparison to other four materials broadly used in modern medical imaging (slope of the linear no-threshold fit was 29.5). The AE is superior from 90 kVp onwards and reaches a value of 29.5 EU at 140 kVp. The same is true for the XLE that, following a flat response, reaches 9×10^{-3} at 90 kVp. Moreover, the spectral matching factors and the respective effective efficiencies (EE) are calculated for a variety of optical sensors. The material exhibits full compatibility with all the flat-panel arrays and most of the photocathodes and Si PMs considered in this work, a factor that proves its suitability for use in state-of-the-art medical imaging applications, such as CT detectors and planar arrays for projection imaging.

Keywords: scintillators; crystals; radiation sensors; medical detectors; cerium bromide

Citation: Linardatos, D.; Michail, C.; Kalyvas, N.; Ninos, K.; Bakas, A.; Valais, I.; Fountos, G.; Kandarakis, I. Luminescence Efficiency of Cerium Bromide Single Crystal under X-ray Radiation. *Crystals* **2022**, *12*, 909. https://doi.org/10.3390/cryst12070909

Academic Editor: Riccardo Cerulli

Received: 27 May 2022
Accepted: 23 June 2022
Published: 25 June 2022

1. Introduction

With the unceasing progress in research on scintillating materials, a number of them have emerged that show great potential for successful implementation in imaging applications. A recent example is cerium bromide ($CeBr_3$), which appears poised to overcome many of the limitations of conventional materials [1–4]. This rare-earth trihalide features a rapid response, negligible afterglow, above-average effective atomic number (45.9) and a convenient emission spectrum for coupling with many optical sensors [5–7]. Mechanically, it is fragile and hygroscopic, necessitating protection from environmental conditions [8,9]. Its main uses include positron emission tomography (PET), dual nuclear and fluoroscopic detectors and gamma-ray spectrometers, etc. [5,10,11]. However, its luminescence properties could make it an alternative material to be considered for X-ray applications as well.

In this work, we chose to evaluate the main luminescence and scintillation properties of a cubic monocrystal of this scintillator. A comparison is also presented versus four other materials targeted to the same field of applications that our group investigated earlier [12–14].

$CdWO_4$, a scintillator similarly free of afterglow, is also endowed with robustness, both mechanically and in terms of hygroscopic resistance, as well as radiation hardness (up to 100 rad). At the same time, it has more than two orders of magnitude greater

decay time (5 μs as opposed to 19 ns) and emits light of greater wavelengths, rendering it incompatible with many photomultiplier tubes (PMTs). Remarkably, it is widely used in modern commercial computed tomography (CT) scanners in medical diagnostics, non-destructive testing (NDT) and other applications [7,15–17].

Lu_2SiO_5:Ce (LSO:Ce) is a relatively dense scintillator (7.4 g/cm^3) with a fast decay time (40 ns). Owing to its high atomic number, it achieves enough stopping power to be applicable in PET energies. An equally effective photon absorber is $Bi_4Ge_3O_{12}$ (BGO), which further exhibits fewer afterglow emissions. Both materials have been reported as well in CT applications employing medical diagnostics X-ray spectral ranges [18–21]. Neither of them suffers from hygroscopicity.

ZnSe:Te, a compound of the II-VI semiconductor group, is non-hygroscopic, mechanically robust, radiation hard and its afterglow is at the same levels as $CdWO_4$. Its atomic number approaches that of copper, a widely used filter for lower-energy X-rays. As a result, ZnSe:Te acts as the detecting element for low-energy photons in dual-energy X-ray detectors. Following this first layer, another, higher-Z material absorbs the photons that come through. Such configurations in the medical imaging field facilitate the diagnosis of tumors, osteoporosis, atherosclerosis, etc. [15,17,22,23]. Further applications include baggage inspection equipment, high-energy physics, space probes and dosimetry [16].

Table 1 summarizes the main luminescence and mechanical properties of the materials in discussion.

Table 1. Scintillators' properties.

	Units	$CeBr_3$	$CdWO_4$	LSO:Ce	ZnSe:Te	BGO
Wavelength of max Emission	nm	380	495	420	640	480
Emission Wavelength Range	nm	340–425	380–800	490–520	525–750	375–650
Decay Time	ns	19	5×10^3	40	$(1–150) \times 10^3$	3×10^2
Light Yield	photons/MeV	6×10^4	$(1.3–2.8) \times 10^4$	2.7×10^3	$(2.8–16.9) \times 10^4$	9×10^3
Photoelectron Yield	% of NaI:Tl	122	30–50	70	31.5–63	15–20
Radiation Length	cm	1.96	1.1	1.1	2.23	1.1
Background Radioactivity	Bq/cm^3	4×10^{-3}	8×10^{-6}	3×10^2		$(7.1–21) \times 10^{-3}$
Refractive Index @ max nm		2.09	2.2–2.3	1.9	2.67	1.8
Afterglow	%	0.1 @ 3 ms	<0.1 @ 2 ms	5 @ 2 ms	<0.05 @ 6 ms	<0.1 @ 2 ms
Density	g/cm^3	5.1	7.9	7.4	5.42	7.13
Effective Atomic Number		45.9	61–66	75	33	74
Melting Point	°C	722	1052	1850	1779	1050
Thermal Conductivity	Wm^{-1} K^{-1}	5.66	4.69	3.02	3.7	11.72
Thermal Expansion Coefficient	C^{-1}	17.7×10^{-6}	10.2×10^{-6}	$(5–11) \times 10^{-6}$	7.6×10^{-6}	7.0×10^{-6}
Mechanical Hardness	Moh	5–6	4–4.5	5.8	4	5
Radiation Hardness	rad	2×10^3	10^2	10^6	10^7	10^2
Hygroscopic		Yes	No	No	No	No
References		[5–7,24]	[25–28]	[7,13,19,29]	[12]	[7,29,30]

The above-mentioned materials in single crystal form of the same 10 mm edge cubic shape were compared under similar conditions in terms of their output signal, absolute efficiency (AE), effective efficiency (EE) and X-ray luminescence efficiency (XLE). Metrics regarding spatial resolution exceed the objective of the present work. The choice of this monocrystal size does not apply to planar detectors, but rather to configurations such as medical X-ray CT; the 10 mm thickness ensures complete photon absorption at the respective energies. Since, according to previous studies [7], the thickness required for nearly complete X-ray absorption is in the order of a few millimeters (2–6 mm), we selected 10 mm for consistency across the results, and to ensure total absorption even of the highest energies used in CT. On the other hand, the luminescence properties investigated herein can be taken into consideration when designing planar detectors for projection imaging. In such a case, the similar conditions under which the measurements were performed ensure that the results (precisely, the relative variations between materials) will be utilizable in future investigations.

2. Materials and Methods

The $CeBr_3$ monocrystal was acquired from Advatech, London, UK [9], had a cubic shape, 10 mm edges, polished surfaces and came encapsulated in an aluminum enclosure. The 'entrance' surface has 0.7 mm Al thickness, while the 'output' consists of a fused silica glass window, 1.93 mm thick. For the precise thickness determinations, the high-resolution non-destructive testing (NDT) Remote RadEye HR CMOS (Teledyne DALSA, ON, Canada) was used. All the crystals in the present work had a cubic shape, 10 mm edges and polished surfaces.

Medical X-ray radiology setting is considered, i.e., aluminum (Al) filtered polyenergetic spectra from medical-type X-ray tubes and high voltages ranging from 50 to 140 kVp. The Aster BK (Assing SpA, Rome, Italy) medical radiography system was used, which consists of the following components: a CMP 200 DR (CPI Inc., Palo Alto, CA, USA) high-frequency X-ray generator and a RTM90HS (IAE SpA, Milano, Italy) X-ray tube in a model C352 housing of the same company. Of the two focal spots (1.2 and 0.6 mm), the larger one was used for our experiments, as well as 20 mm Al filtering in order to approximate a typical human chest.

The output signal in terms of emitted light energy per unit area $\left(\dot{\Psi}_\Lambda\right)$ was determined for a series of X-ray exposure rates. In order to obtain the crystal's emitted light energy, an integrating sphere (Newport Corp., Irvine, CA, USA, model Oriel 70451) was used, in the configuration described in [12]. The cubic crystal's "back" surface lays on the sphere's entrance window. The collected light is detected by a PMT (EMI, London, UK, model 9798 with S20 photocathode with extended sensitivity) connected as a biased photodiode and its current is sensed by a sub-femtoamp electrometer (Keithley, Cleveland, OH, USA, model 6430) [12]. The distance between the entrance surface of the cubic scintillator and the X-ray tube focal spot was 72.5 cm. The X-ray dose rates were provided by a dosimeter (RTI, Mölndal, Sweden, model Piranha P100B).

The output signal or light energy flux is given by [12]:

$$\dot{\Psi}_\lambda = \frac{i_{elec}}{S \cdot \eta_p \cdot \alpha_s \cdot c_g}, \tag{1}$$

where i_{elec} is the PMT current, as measured by the electrometer, in pA. S is the irradiated area of the scintillator, in mm^2. n_p is the photocathode's peak photosensitivity, in $pA \cdot W^{-1}$. α_s is the spectral matching factor (SMF) between the crystal's emitted spectrum and the photocathode's spectral response. c_g is the geometric light collection efficiency of the experimental setup, including the integrating sphere; estimated as 15.6 for our specific geometry. The light energy flux is expressed in $\mu W \cdot m^{-2}$.

Absolute efficiency is the ratio of the crystal's light energy flux to the X-ray exposure rate, i.e.:

$$AE = \eta_A = \frac{\dot{\Psi}_\lambda}{\dot{X}}, \tag{2}$$

where the exposure rate is expressed in $mR \cdot s^{-1}$ and eventually the AE unit is $1\ \left(\mu W \cdot m^{-2}\right) / \left(mR \cdot s^{-1}\right) = 1\ EU$.

The effective efficiency is the AE multiplied with the spectral matching factor α_s of the respective detector that is coupled to the scintillator [31]:

$$EE = \eta_{eff} = \eta_A \cdot \alpha_s \tag{3}$$

$$\alpha_s = \frac{\int S_p(\lambda) \cdot S_D(\lambda) \cdot d\lambda}{\int S_p(\lambda) \cdot d\lambda}, \tag{4}$$

where λ denotes photon wavelength. S_p is the spectrum of the light emitted by the scintillator. S_D is the spectral sensitivity of the optical detector.

The effective efficiency was calculated for various commercial detectors, while the crystal's emission spectrum was measured by a grating spectrometer (Ocean Optics HR2000) under UV excitation.

The X-ray luminescence efficiency (η_Ψ) is the ratio of the crystal's emitted light energy flux over the X-ray energy flux [32], i.e., $\eta_\Psi = \dot{\Psi}_\lambda / \dot{\Psi}_0$. It has no units of measure and expresses which part of the incident energy is converted to light.

3. Results and Discussion

The output signal versus X-ray exposure rate for all materials is plotted in Figure 1. Within the exposure range of interest for medical diagnostics employed in our experiments, i.e., up to 370 mR/s, all responses are linear. All R^2 values (coefficient of determination) of the linear no-threshold fits are at least 0.99. The superiority of $CeBr_3$ and $CdWO_4$ in terms of their light yield is denoted by the increased slopes.

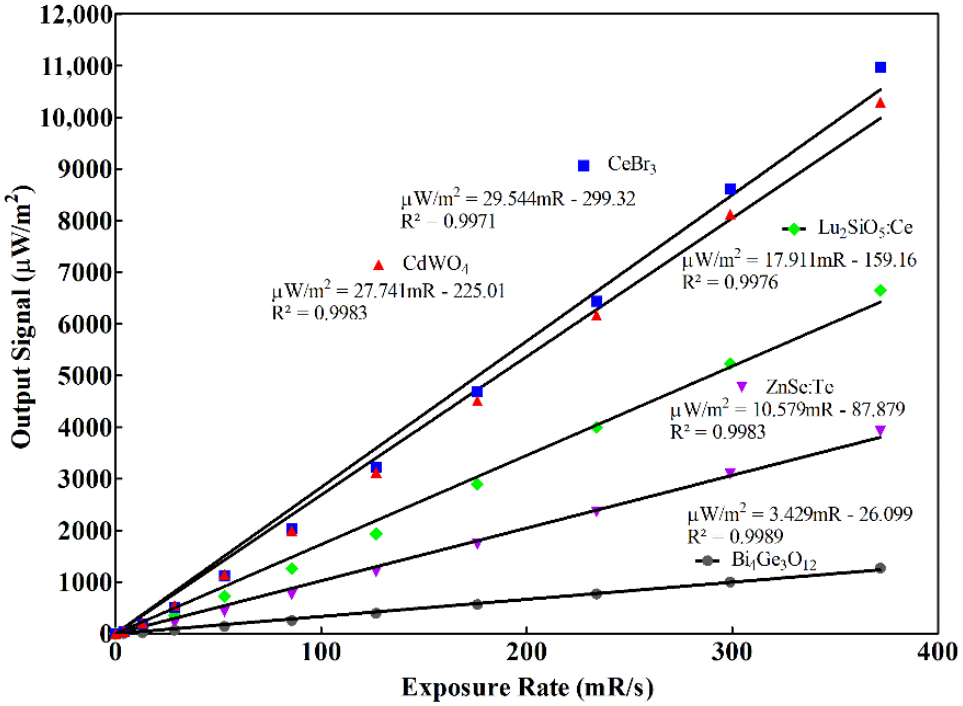

Figure 1. Output signal versus exposure rate.

Absolute luminescence efficiency versus the X-ray tube's high voltage is depicted in Figure 2 for each scintillator. Every material's AE increases constantly with increasing high voltage. The relationship is linear for $CeBr_3$ within the intervals 50–80 kVp and 100–140 kVp, albeit at different slopes. $CeBr_3$ and $CdWO_4$ attain similarly high AE values, regardless of the former's lower effective Z and density, thus demonstrating its excellent performance at light yield capacity. $CeBr_3$ reaches 29.5 EU at 140 kVp spectrum, the largest value of all examined materials. In the graph of the output signal versus exposure rate (Figure 1), the fitted lines' slopes are in accordance with the relationship between the scintillators' AE values (Figure 2). The decreased slope of the BGO line corresponds to inferior AE values. $CeBr_3$ and $CdWO_4$ output signal slopes stand higher and close to each other, similarly to the respective absolute efficiencies. Moreover, LSO:Ce and ZnSe:Te absolute efficiency curves, like the respective output signal slopes, stand halfway between.

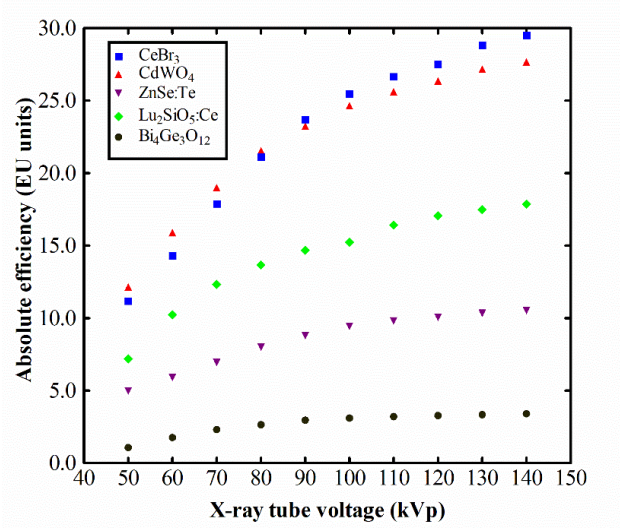

Figure 2. Absolute efficiency versus X-ray tube high voltage.

In order to calculate effective efficiency, the spectral matching factor is needed. The necessary spectral responses of several commercial light sensors are presented in Figures 3 and 4 along with the emitted spectrum of $CeBr_3$. The respective SMFs of the various combinations of $CeBr_3$ are summarized in [33].

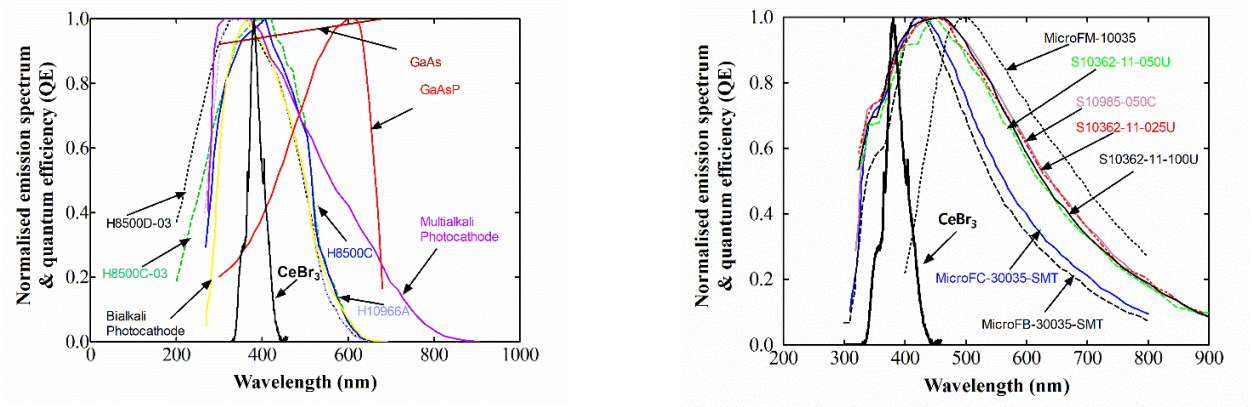

(**a**) (**b**)

Figure 3. $CeBr_3$ spectral matching with: (**a**) photocathodes; (**b**) silicon photomultipliers.

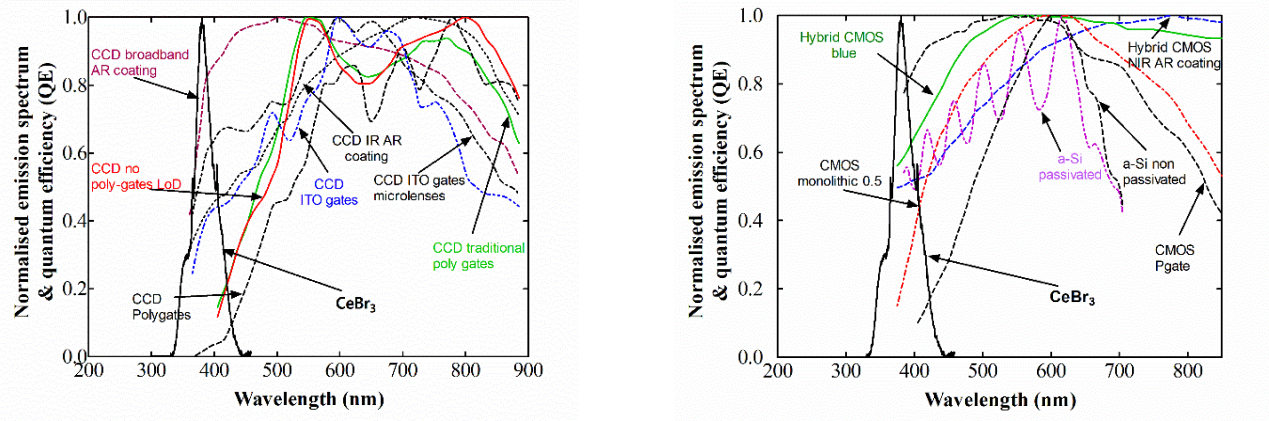

(**a**) (**b**)

Figure 4. $CeBr_3$ spectral matching with: (**a**) charge-coupled-devices; (**b**) complementary metal-oxide semiconductors.

The EE values versus the X-ray tube high voltage are depicted in Figures 5 and 6, for all the chosen detectors above.

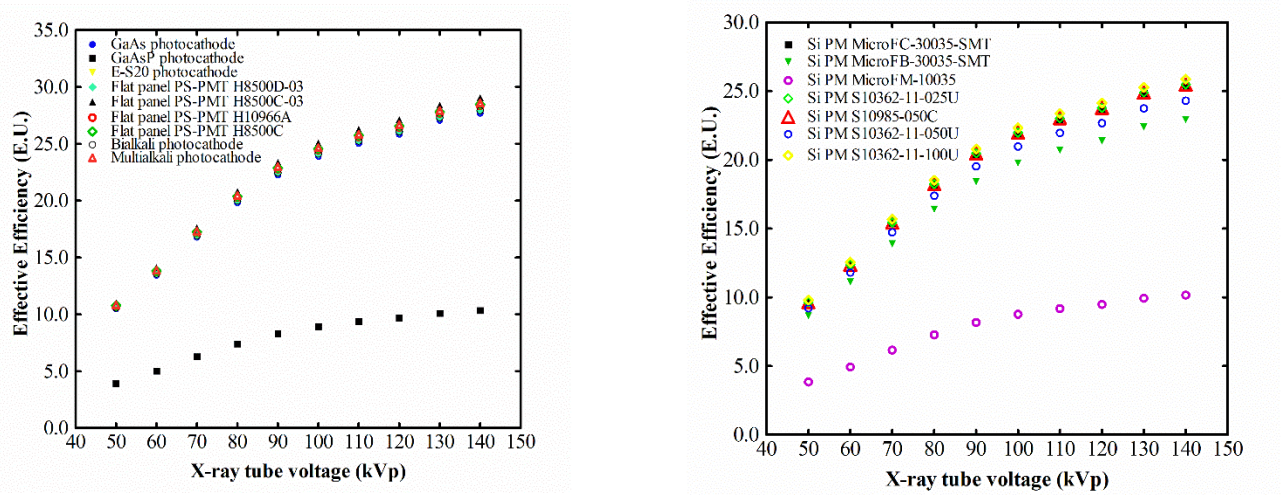

(**a**) (**b**)

Figure 5. $CeBr_3$ effective efficiency with: (**a**) photocathodes; (**b**) silicon photomultipliers.

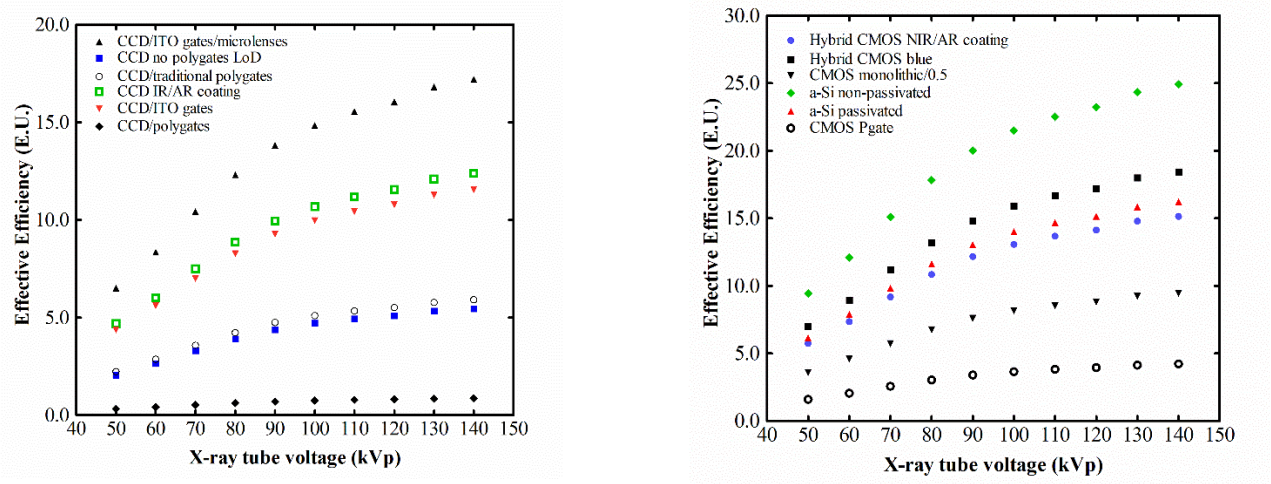

(**a**) (**b**)

Figure 6. $CeBr_3$ effective efficiency with: (**a**) charge-coupled-devices; (**b**) complementary metal-oxide semiconductors.

As it is expected from their SMFs, the EE approaches the AE for most photocathodes and some of the silicon PMs calculated. Nearly every photocathode and flat-panel array exhibit full compatibility in detecting the scintillator's light, with the exception of the GaAsP photocathode. For example, the EE of the combination of the flat-panel FP H8500C-03 with $CeBr_3$ reaches 28.9 EU at 140 kVp, where AE is 29.5 EU. The combination of $CeBr_3$ with most Si PMs attains the same levels of efficiency, yet to a lesser degree. As far as CCDs and CMOSs are concerned, the compatibility is reduced, with the sole exception of the a-Si passivated CMOS. The latter reaches 24 EU at the maximum tube voltage. For all the other calculated CCDs and CMOSs, the maximum attained effective efficiency rests below 25 EU at 140 kVp. The $CeBr_3$ compatibility with CCDs and CMOSs may seem reduced in comparison with PMTs and Si PMs, however, the respective EE values are comparable or even better than those of the other scintillators in discussion. For example ZnSe:Te EE with CCD/CMOSs reaches up to 10 EU at best [12]; $CdWO_4$ with CCDs reaches 21 EU, while with CMOSs 26 EU [14].

The XLE of the crystals under investigation is shown in Figure 7, versus the selected high voltage.

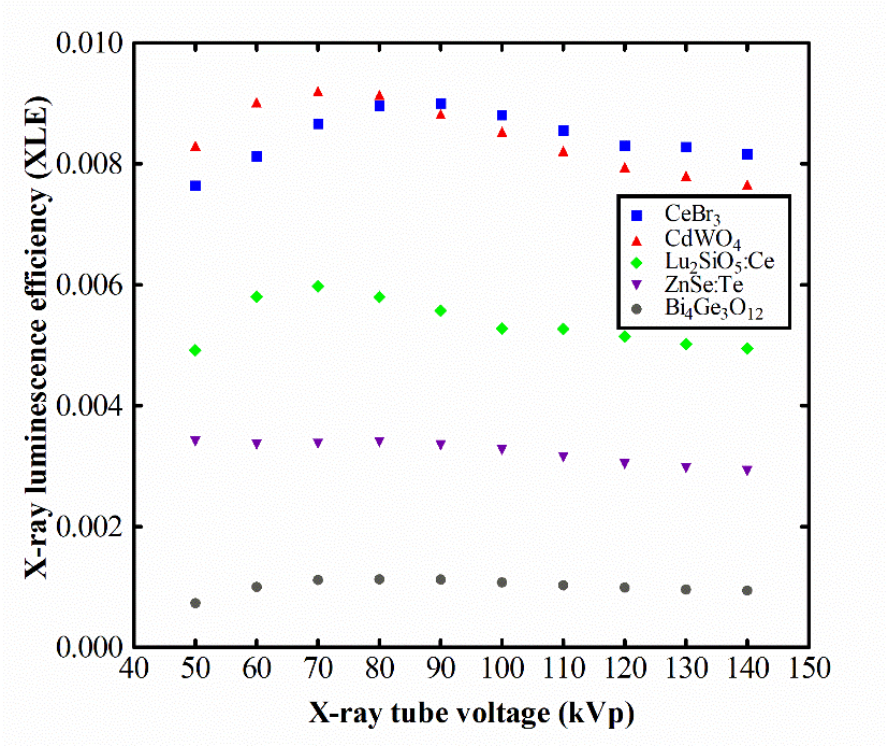

Figure 7. X-ray luminescence efficiency versus tube high voltage.

$CeBr_3$ and $CdWO_4$ exhibit similar XLE responses, both starting from ~8 × 10^{-3} at 50 kVp, slightly culminating (~9 × 10^{-3}) at 90 kVp and returning to ~8 × 10^{-3} at 140 kVp. Their attenuation coefficients (visible in Figure 8) present local peaks, namely the photoelectric absorption edges, at the energies of ~40 keV and ~69 keV, respectively. The other materials remain below 6 × 10^{-3} throughout the whole examined voltage range.

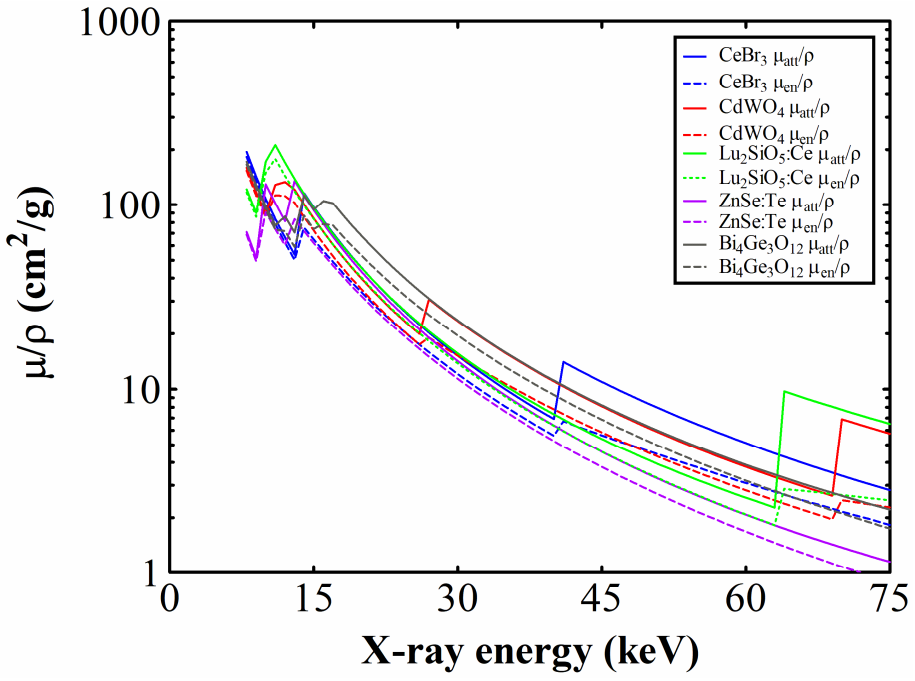

Figure 8. Compounds' attenuation coefficients.

The μ_{att}, i.e., the probability that an X-ray photon is absorbed due to any kind of interaction within the crystal and the μ_{en}, i.e., the probability that a photon's energy is transferred to electrons in the material are plotted in Figure 8 for the energy range in question. It is noted that the effective energy of a filtered spectrum from a 140 kVp X-ray tube approximates 74 keV.

The X-ray luminescence efficiency of a scintillator, expressing its capacity to convert the incident X-ray energy to visible light, is a crucial performance metric for energy integrating detectors. Medical X-ray radiology utilizes this particular type of detector, in which the resulting output signal is a function of the total energy that is absorbed by the scintillating material. The magnitude of this efficiency measure across the various X-ray spectra depends on the following properties of the material. First, the quantum detection efficiency, i.e., the fraction of the incident X-ray photons absorbed by the scintillator. Second, the intrinsic X-ray to light conversion efficiency, i.e., the part of the absorbed X-ray energy that is converted to light energy. Third, the light transmission efficiency, which indicates the probability that the light energy from the point of interaction will escape the crystal's mass [32].

$CeBr_3$ exhibits optimum performance with regard to XLE for X-ray spectra above 90 kVp, in comparison to the other materials discussed in this work. Below 80 kVp, $CeBr_3$ is slightly less efficient than $CdWO_4$, yet maintains high levels of XLE (always at least 7.6×10^{-3}). From 90 kVp onwards (i.e., CT-pertinent energies) the situation inverses. This uniformity in response within the examined spectral range (min to max difference is 16%) facilitates its practical implementation in medical imaging systems.

It is worth mentioning here that owing to $CeBr_3$'s necessity for encapsulation, its emitted light was measured after going through the glass window. This inevitably causes a fraction of the light photons to be attenuated, which indicatively, in the investigation of Quarati et al. [34] meant a reduction of the light yield average from 60,000 ph/MeV of bare samples to 45,000 ph/MeV of encapsulated ones. Further, despite the larger light yield of $CeBr_3$ compared to $CdWO_4$, the higher density and effective Z of the latter leads to more effective X-ray absorption, especially at lower energies where the photoelectric effect prevails. Such light yield data are given in Table 1 as an indication only, since they are determined under completely different experimental conditions (i.e., single-energy gamma ray photons of significantly higher energy than X-ray tube generated photons and different measuring equipment). On the other hand, published light yield values differ significantly from one publication to another [28]. In addition, the different emission wavelengths suggest different optical transmission and escape properties; factors that contribute as well to the materials' luminescence efficiencies.

4. Conclusions

The objective of this study was to examine the luminescence and scintillation properties of a $CeBr_3$ single crystal under typical X-ray radiology conditions (medical X-ray tube, spectra in the range 50–140 kVp, human chest equivalent filtering). The main conclusions are that: (i) The luminescence output of $CeBr_3$ was found comparable to $CdWO_4$ and clearly higher than LSO:Ce, ZnSe:Te and certainly BGO. At an X-ray tube energy of 140 kVp, its luminescence output reached 29.5 EU. (ii) $CeBr_3$ shows X-ray luminescence efficiency maximum of 9×10^{-3} at 90 kVp. From this energy and beyond, it shows higher XLE values than all other materials in this study. (iii) $CeBr_3$ emitted light wavelength exhibits full compatibility with all the flat-panel arrays, most of the photocathodes and Si PMs considered in this work.

In addition to these advantageous luminescence characteristics of $CeBr_3$, there should be taken into consideration the detrimental effect of the encapsulation window that diminishes the luminescence photons that finally escape. Certainly, the encapsulation of hygroscopic materials is a prerequisite. Nevertheless, in the design of a radiation detector, the whole configuration could be enclosed in a hermetic seal. The scintillator would be in direct optical contact (e.g., via optical grease or similar means) with the optical sensor and

nearly the entire luminescence output would be collected, further benefiting $CeBr_3$ in the luminescence parameters comparison to its counterparts.

Moreover, $CeBr_3$′s rapid response, negligible afterglow, above-average density and effective atomic number verdict that such crystals should be considered for use in CT detectors or planar arrays for projection imaging. Incorporation in glass matrix for the engineering of structured scintillators has been reported [35,36], as well as pixelated arrays of this material [37].

On the other hand, its hygroscopicity and fragility should be taken into consideration during the designing phase of the final product, e.g., moisture-tight enclosures (NaI:Tl in gamma cameras), shock-dampening mechanisms, etc. These factors would certainly exclude this compound from applications where high mechanical and radiation burden could eventually hamper its characteristics, such as space and calorimetry.

Author Contributions: Conceptualization, D.L. and C.M.; Data curation, D.L., C.M., N.K., G.F. and I.K.; Formal analysis, D.L., C.M., N.K., K.N. and A.B.; Investigation, D.L., C.M., N.K., I.V. and G.F.; Methodology, D.L., C.M., N.K., I.V., G.F. and I.K.; Project administration, C.M. and G.F.; Resources, K.N. and A.B.; Software, D.L.; Supervision, C.M.; Validation, N.K. and I.K.; Visualization, I.V.; Writing—original draft, D.L. and C.M.; Writing—review and editing, N.K., I.V. and I.K. All authors have read and agreed to the published version of the manuscript.

Funding: This research received no external funding.

Data Availability Statement: Data is contained within the article.

Conflicts of Interest: The authors declare no conflict of interest.

References

1. Wei, H.; Martin, V.; Lindsey, A.; Zhuravleva, M.; Melcher, C.L. The Scintillation Properties of $CeBr_{3-x}Cl_x$ Single Crystals. *J. Lumin.* **2014**, *156*, 175–179. [CrossRef]
2. Loyd, M.; Stand, L.; Rutstrom, D.; Wu, Y.; Glodo, J.; Shah, K.; Koschan, M.; Melcher, C.L.; Zhuravleva, M. Investigation of $CeBr_{3-x}I_x$ Scintillators. *J. Cryst. Growth* **2020**, *531*, 125365. [CrossRef]
3. Kandarakis, I. Luminescence in Medical Image Science. *J. Lumin.* **2016**, *169*, 553–558. [CrossRef]
4. Xie, S.; Zhang, X.; Zhang, Y.; Ying, G.; Huang, Q.; Xu, J.; Peng, Q. Evaluation of Various Scintillator Materials in Radiation Detector Design for Positron Emission Tomography (PET). *Crystals* **2020**, *10*, 869. [CrossRef]
5. Koppert, W.J.C.; Dietze, M.M.A.; Velden, S.; Steenbergen, J.H.L.; Jong, H.W.A.M. A Comparative Study of NaI(Tl), $CeBr_3$ and CZT for Use in a Real-Time Simultaneous Nuclear and Fluoroscopic Dual-Layer Detector. *Phys. Med. Biol.* **2019**, *64*, 135012. [CrossRef] [PubMed]
6. Van Loef, E.V.; Shah, K.S. Advances in Scintillators for Medical Imaging Applications. In Proceedings of the SPIE, San Diego, CA, USA, 12 September 2014; p. 92140A.
7. Lecoq, P. Development of New Scintillators for Medical Applications. *Nucl. Instrum. Methods Phys. Res. Sect. Accel. Spectrometers Detect. Assoc. Equip.* **2016**, *809*, 130–139. [CrossRef]
8. Higgins, W.M.; Churilov, A.; Loef, E.; Glodo, J.; Squillante, M.; Shah, K. Crystal Growth of Large Diameter $LaBr_3$:Ce and $CeBr_3$. *J. Cryst. Growth* **2008**, *310*, 2085–2089. [CrossRef]
9. Advatech UK. Advatech UK—$CeBr_3$. Available online: https://www.advatech-uk.co.uk/cebr3.html (accessed on 4 March 2022).
10. Otaka, Y.; Shimazoe, K.; Mitsuya, Y.; Uenomachi, M.; Seng, F.W.; Kamada, K.; Yoshikawa, A.; Sakuragi, S.; Binder, T.; Takahashi, H. Performance Evaluation of Liquinert-Processed $CeBr_3$ Crystals Coupled With a Multipixel Photon Counter. *IEEE Trans. Nucl. Sci.* **2020**, *67*, 988–993. [CrossRef]
11. Kaburagi, M.; Shimazoe, K.; Kato, M.; Kurosawa, T.; Kamada, K.; Kim, K.J.; Yoshino, M.; Shoji, Y.; Yoshikawa, A.; Takahashi, H.; et al. Gamma-Ray Spectroscopy with a $CeBr_3$ Scintillator under Intense γ-Ray Fields for Nuclear Decommissioning. *Nucl. Instrum. Methods Phys. Res. Sect. Accel. Spectrometers Detect. Assoc. Equip.* **2021**, *988*, 164900. [CrossRef]
12. Linardatos, D.; Konstantinidis, A.; Valais, I.; Ninos, K.; Kalyvas, N.; Bakas, A.; Kandarakis, I.; Fountos, G.; Michail, C. On the Optical Response of Tellurium Activated Zinc Selenide ZnSe:Te Single Crystal. *Crystals* **2020**, *10*, 961. [CrossRef]
13. Valais, I.; Michail, C.; David, S.; Nomicos, C.D.; Panayiotakis, G.S.; Kandarakis, I. A Comparative Study of the Luminescence Properties of LYSO:Ce, LSO:Ce, GSO:Ce and BGO Single Crystal Scintillators for Use in Medical X-Ray Imaging. *Phys. Med.* **2008**, *24*, 122–125. [CrossRef] [PubMed]
14. Michail, C.M.; Koukou, V.; Martini, N.; Saatsakis, G.; Kalyvas, N.; Bakas, A.; Kandarakis, I.; Fountos, G.; Panayiotakis, G.; Valais, I. Luminescence Efficiency of Cadmium Tungstate ($CdWO_4$) Single Crystal for Medical Imaging Applications. *Crystals* **2020**, *10*, 429. [CrossRef]

15. Grinyov, B.V.; Ryzhikov, V.D.; Naydenov, S.V.; Opolonin, A.D.; Lisetskaya, E.K.; Galkin, S.N.; Lecoq, P. Medical Dual-Energy Imaging of Bone Tissues Using ZnSe-Based Scintillator-Photodiode Detectors. In Proceedings of the 2006 IEEE Nuclear Science Symposium Conference Record, San Diego, CA, USA, 29 October–4 November 2006; IEEE: San Diego, CA, USA, 2006; pp. 1945–1949.
16. Ryzhikov, V.D.; Opolonin, A.D.; Pashko, P.V.; Svishch, V.M.; Volkov, V.G.; Lysetskaya, E.K.; Kozin, D.N.; Smith, C. Instruments and Detectors on the Base of Scintillator Crystals ZnSe(Te), CWO, CsI(Tl) for Systems of Security and Customs Inspection Systems. *Nucl. Instrum. Methods Phys. Res. Sect. Accel. Spectrometers Detect. Assoc. Equip.* **2005**, *537*, 424–430. [CrossRef]
17. Shefer, E.; Altman, A.; Behling, R.; Goshen, R.; Gregorian, L.; Roterman, Y.; Uman, I.; Wainer, N.; Yagil, Y.; Zarchin, O. State of the Art of CT Detectors and Sources: A Literature Review. *Curr. Radiol. Rep.* **2013**, *1*, 76–91. [CrossRef]
18. Hagiwara, O.; Sato, E.; Oda, Y.; Yamaguchi, S.; Sato, Y.; Matsukiyo, H.; Enomoto, T.; Watanabe, M.; Kusachi, S. Dual-Energy X-Ray Computed Tomography Scanner Using Two Different Energy-Selection Electronics and a Lutetium-Oxyorthosilicate Photomultiplier Detector. *Int. J. Med. Phys. Clin. Eng. Radiat. Oncol.* **2017**, *6*, 266–279. [CrossRef]
19. Kastengren, A. Thermal Behavior of Single-Crystal Scintillators for High-Speed X-Ray Imaging. *J. Synchrotron Radiat.* **2019**, *26*, 205–214. [CrossRef]
20. Lohrabian, V.; Kamali-Asl, A.; Harvani, H.G.; Hosseini Aghdam, S.R.; Arabi, H.; Zaidi, H. Comparison of the X-Ray Tube Spectrum Measurement Using BGO, NaI, LYSO, and HPGe Detectors in a Preclinical Mini-CT Scanner: Monte Carlo Simulation and Practical Experiment. *Radiat. Phys. Chem.* **2021**, *189*, 109666. [CrossRef]
21. Nassalski, A.; Kapusta, M.; Batsch, T.; Wolski, D.; Mockel, D.; Enghardt, W.; Moszynski, M. Comparative Study of Scintillators for PET/CT Detectors. *IEEE Trans. Nucl. Sci.* **2007**, *54*, 3–10. [CrossRef]
22. Martini, N.; Koukou, V.; Fountos, G.; Michail, C.; Bakas, A.; Kandarakis, I.; Speller, R.; Nikiforidis, G. Characterization of Breast Calcification Types Using Dual Energy X-Ray Method. *Phys. Med. Biol.* **2017**, *62*, 7741–7764. [CrossRef]
23. Koukou, V.; Martini, N.; Fountos, G.; Michail, C.; Bakas, A.; Oikonomou, G.; Kandarakis, I.; Nikiforidis, G. Application of a Dual Energy X-Ray Imaging Method on Breast Specimen. *Results Phys.* **2017**, *7*, 1634–1636. [CrossRef]
24. Drozdowski, W.; Dorenbos, P.; Bos, A.J.J.; Owens, A.; Richaud, D. Gamma Radiation Hardness of Ø1″ × 1″ $LaBr_3$:Ce, $LaCl_3$:Ce, and $CeBr_3$ Scintillators. In Proceedings of the 2008 IEEE Nuclear Science Symposium Conference Record, Dresden, Germany, 19–25 October 2008; pp. 2856–2858.
25. van Eijk, C.W.E. Inorganic Scintillators in Medical Imaging. *Phys. Med. Biol.* **2002**, *47*, R85–R106. [CrossRef] [PubMed]
26. Lecoq, P.; Annenkov, A.; Gektin, A.; Korzhik, M.; Pedrini, C. *Inorganic Scintillators for Detector Systems: Physical Principles and Crystal Engineering*; Lecoq, P., Ed.; Particle Acceleration and Detection; Springer: Berlin, Germany, 2006; ISBN 978-3-540-27766-8.
27. Kobayashi, M.; Ishii, M.; Usuki, Y.; Yahagi, H. Cadmium Tungstate Scintillators with Excellent Radiation Hardness and Low Background. *Nucl. Instrum. Methods Phys. Res. Sect. Accel. Spectrometers Detect. Assoc. Equip.* **1994**, *349*, 407–411. [CrossRef]
28. Bardelli, L.; Bini, M.; Bizzeti, P.G.; Carraresi, L.; Danevich, F.A.; Fazzini, T.F.; Grinyov, B.V.; Ivannikova, N.V.; Kobychev, V.V.; Kropivyansky, B.N.; et al. Further Study of $CdWO_4$ Crystal Scintillators as Detectors for High Sensitivity Experiments: Scintillation Properties and Pulse-Shape Discrimination. *Nucl. Instrum. Methods Phys. Res. Sect. Accel. Spectrometers Detect. Assoc. Equip.* **2006**, *569*, 743–753. [CrossRef]
29. Kozma, P.; Kozma, P. Radiation Sensitivity of GSO and LSO Scintillation Detectors. *Nucl. Instrum. Methods Phys. Res. Sect. Accel. Spectrometers Detect. Assoc. Equip.* **2005**, *539*, 132–136. [CrossRef]
30. Grigoriev, D.N.; Kazanin, V.F.; Kuznetcov, G.N.; Novoselov, I.I.; Schotanus, P.; Shavinski, B.M.; Shepelev, S.N.; Shlegel, V.N.; Vasiliev, Y.V. Alpha Radioactive Background in BGO Crystals. *Nucl. Instrum. Methods Phys. Res. Sect. Accel. Spectrometers Detect. Assoc. Equip.* **2010**, *623*, 999–1001. [CrossRef]
31. Valais, I.; Kandarakis, I.S.; Nikolopoulos, D.N.; Sianoudis, I.A.; Dimitropoulos, N.; Cavouras, D.A.; Nomicos, C.D.; Panayiotakis, G.S. Luminescence Efficiency of (Gd_2SiO_5:Ce) Scintillator under X-Ray Excitation. In Proceedings of the IEEE Symposium Conference Record Nuclear Science, Rome, Italy, 16–22 October 2004; IEEE: Rome, Italy, 2004; Volume 5, pp. 2737–2741.
32. Michail, C.M.; Valais, I.; Fountos, G.; Bakas, A.; Fountzoula, C.; Kalyvas, N.; Karabotsos, A.; Sianoudis, I.; Kandarakis, I. Luminescence Efficiency of Calcium Tungstate ($CaWO_4$) under X-Ray Radiation: Comparison with Gd_2O_2S:Tb. *Measurement* **2018**, *120*, 213–220. [CrossRef]
33. Linardatos, D.; Velissarakos, K.; Valais, I.; Fountos, G.; Kalyvas, N.; Michail, C. Cerium Bromide Single-Crystal X-Ray Detection and Spectral Compatibility Assessment with Various Optical Sensors. *Mater. Des. Process. Commun.* **2022**, *2022*, 7008940. [CrossRef]
34. Quarati, F.G.A.; Dorenbos, P.; van der Biezen, J.; Owens, A.; Selle, M.; Parthier, L.; Schotanus, P. Scintillation and Detection Characteristics of High-Sensitivity $CeBr_3$ Gamma-Ray Spectrometers. *Nucl. Instrum. Methods Phys. Res. Sect. Accel. Spectrometers Detect. Assoc. Equip.* **2013**, *729*, 596–604. [CrossRef]

35. Lin, Z.; Lv, S.; Yang, Z.; Qiu, J.; Zhou, S. Structured Scintillators for Efficient Radiation Detection. *Adv. Sci.* **2022**, *9*, 2102439. [CrossRef]
36. Barta, M.B.; Nadler, J.H.; Kang, Z.; Wagner, B.K.; Rosson, R.; Cai, Y.; Sandhage, K.H.; Kahn, B. Composition Optimization of Scintillating Rare-Earth Nanocrystals in Oxide Glass–Ceramics for Radiation Spectroscopy. *Appl. Opt.* **2014**, *53*, D21. [CrossRef]
37. Ackermann, U.; Eschbaumer, S.; Bergmaier, A.; Egger, W.; Sperr, P.; Greubel, C.; Löwe, B.; Schotanus, P.; Dollinger, G. Position and Time Resolution Measurements with a Microchannel Plate Image Intensifier: A Comparison of Monolithic and Pixelated $CeBr_3$ Scintillators. *Nucl. Instrum. Methods Phys. Res. Sect. Accel. Spectrometers Detect. Assoc. Equip.* **2016**, *823*, 56–64. [CrossRef]